ORIGINAL PAPER

Effect of a Spatially Fluctuating Heating of Particles in a Plasma Spray Process

T. Zhu[1] · M. Baeva[1] · H. Testrich[1] · T. Kewitz[1] · R. Foest[1]

Abstract

The work is concerned with the effect of a spatially fluctuating heating of Al_2O_3 particles with diameters of 5–120 μm during a plasma spray process. A plasma jet is generated in a mixture of Ar (40 NLPM) and H_2 (14 NLPM) and in pure Ar at an electric current of 600 A. The tracing of the injected particles in the plume region of the plasma jets is considered in the framework of a three-dimensional model taking into account a turbulent fluid flow. It is shown that the heat source for the injected particles exhibits a well pronounced spatially fluctuating structure due to the enhancement of the thermal conductivity resulting from dissociation and ionization of the molecular gas in the temperature range of 2500–4000 K and 13,000–14,000 K, respectively. During their travel towards the substrate, the particles are therefore repeatedly heated in the gas mixture in contrast to the case of pure argon. Particles injected in the gas mixture reach the substrate with a higher average temperature and velocity.

Introduction

Plasma spraying is one of the most versatile techniques for the preparation and production of functional coatings (e.g. heat-, bearing- and corrosion-resistant) in industrial applications [1, 2]. The process is attractive for both industrial and academic fields due to the high temperature, velocity and energy density that can be achieved.

In plasma spraying, the electric arc generated inside the plasma torch heats and accelerates the working gas due to the Joule heating, Lorentz and drag forces. Gas temperatures of about 10,000–15,000 K and velocities from several 100 ms^{-1} up to about 2000 ms^{-1} can be reached at the torch exit [2, 3]. A hot plasma jet is pushed out of the torch nozzle. It expands to form a plume in the outer region and impinges onto a substrate. A powder is fed by a carrier gas into the plasma jet through an injector placed

✉ M. Baeva
baeva@inp-greifswald.de

1   Leibniz Institute for Plasma Science and Technology, Felix-Hausdorff-Str. 2, 17489 Greifswald, Germany

usually a few mm away from the torch axis and the torch exit. The particles of the powder are heated by the plasma jet and can be deposited on the substrate.

The properties of the coatings produced in the plasma spray process are affected by factors such as the plasma torch operation, the state of the generated plasma jet, the properties of the injected powder, and the placement of the substrate [4–13]. In order to improve the quality and productivity of functional coatings, many studies have been carried out over the past few decades. Some studies have focused on the suppression of arc instabilities [14], the extension of the lifetime of the electrodes [15–17], the high-precision control on the plasma jet [18], the optimization of the plasma torch design for higher energy fluxes [19, 20], the interaction between the fed particles and the plasma jet [21, 22], and the combination of plasma spray process with machine learning algorithms [23, 24], just to mention a few of the topics.

Numerical simulations on plasma spraying have been a topic of interest over the course of many years. Since the 1980s, the simulations have been extended from a single particle to multiple particles, to two and three dimensions in a single gas and in gas mixtures [25–43]. The effect of a time-fluctuating plasma jet on the particle injection has been studied by Meillot [42]. Li et.al [12, 13] have applied a three-dimensional and turbulent model for the plasma jet to study the effects of random turbulent fluctuation of the plasma jet on in-flight Ni particles. A series of works has been done by Bobzin et al. [9, 10] on 3D multi-arc spraying device, considering the two-way coupling between plasma jet and fed particles (Al_2O_3) in the conservation equations of mass, momentum and energy. A resolution of the in-flight particle is performed in [21] for consideration of the heat transfer inside the particle. A special attention has been paid on the dispersion of the injection parameters [7, 8] in order to approach a real commercial application as well as on the analysis of the coatings on the substrate plane. Bobzin et al. [10] has included the pipe for powder feeding in the computational domain to account for the injection dispersion of the particles. The dispersion of particles in their size has been considered but the diameter range has been restricted to (35–73.9 μm) in [43] and to (20.1–60.4 μm) in [10] in order to avoid effects of the turbulent dispersion on particles with a diameter below 10 μm [44]. These effects have been studied by Li et al. [12, 13] for Ni particles with fixed diameters of 5 μm, 10 μm, and 20 μm. The results obtained showed that turbulent dispersion affects the particle trajectories even for a value of the particle diameter of 20 μm.

It is known that admixtures of H_2 and N_2 to Ar are used in industrial plasma spraying in order to increase the enthalpy of the working gas. The behavior of the particles fed into the plasma jet of mixtures Ar-He [39], Ar-H_2 [25–28, 30, 34, 36, 37, 41], Ar-N_2 [29, 35] or even the ternary mixture of Ar-He-H_2 have been studied. It has been shown that as a result of the higher thermal conductivity of mixtures of Ar with molecular gases, the particles are stronger heated than in pure Ar. The temperature dependence of thermal conductivity of the mixture is characterized by maxima, which are related to the dissociation of the molecules [45]. The particles injected into the plasma jet, therefore, will cross a fluctuating field of thermal conductivity and experience some kind of multiple heating acts. To the best of authors' knowledge, this effect has not been considered in detail so far.

In a recent work [46], we reported on a self-consistent coupling of the thermionic cathode and its non-equilibrium boundary layer with the bulk plasma in the state of local thermodynamic equilibrium inside the plasma torch Oerlikon Metco F4MB-XL [47], as well as on the impact of the flow description on the predictive capability of a model of the plasma torch. It was shown that the cathode-plasma coupling is essential for the agreement with experimental data with respect to the arc voltage and electric

power, while the high Mach number fluid flow approach improves the prediction with respect to the thermal efficiency of the plasma torch.

The present work is aimed at the simulation of the particles injected into the plasma jet outside the plasma spray torch Oerlikon Metco F4MB-XL, which can be operated in pure Ar and in mixtures Ar/H$_2$ and Ar/N$_2$ [47]. The behavior of the particles in the case of a fluctuating thermal conductivity in the plasma jet generated in a mixture of Ar and H$_2$ is studied and compared to that in pure Ar, accounting for turbulent dissipation for all particle sizes. For this purpose, a three-dimensional model of a turbulent plasma jet and the carrier gas flow is employed and the injected particles Al$_2$O$_3$ are followed until their impact onto the substrate. A random sampling of the particle release with respect to the position on the injector's exit, the angle and velocity of injection, and the size of the particles is considered. The behavior of the particles reaching the substrate is characterized by the K-Sommerfeld number.

The paper is organized as follows: the main features of the 3D model are given in 'Computational methods'; results of the confirmed cases are discussed in 'Results and Discussion'; Concluding remarks are given in 'Conclusion'. Supplementary data and validation results are given in Appendices A–E.

Computational Methods

The schematic of the problem under consideration is shown in Fig. 1. The plasma jet generated in the DC torch is pushed out of the torch nozzle BB′ and expands towards the substrate DD′. Powder particles are released into the plasma jet through the exit FG of the injector. The computational domain is a half of a cylinder with a length of 120 mm and a radius of 48 mm. The injector has a diameter of 1.5 mm and is placed at a distance of 6 mm away from the nozzle and 10 mm away from the torch axis. In the problem that we consider it can be assumed that the effect of the particles on the plasma jet is negligible [30]. The problems of the particle motion and the plasma jet flow calculation are separate problems. The particles move in a known background, which is pre-computed.
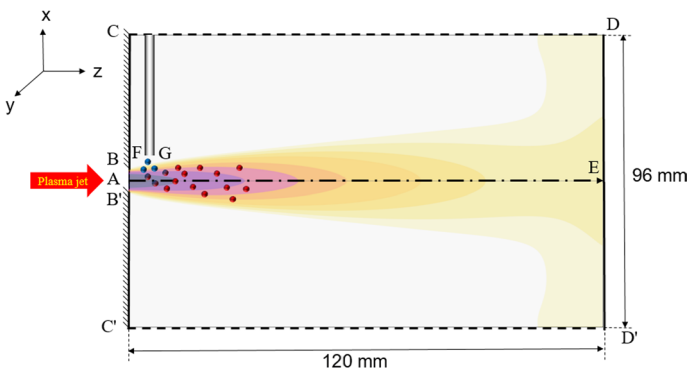
Fig. 1 Schematic of the computational domain with the particle injector

Motion of the Injected Particles

The force acting on a particle that is moving in the fluid background can be expressed by the Newton's second law.

$$\frac{d(m_p \boldsymbol{v})}{dt} = \boldsymbol{F}_d + \boldsymbol{F}_g + \boldsymbol{F}_{tp}, \tag{1}$$

where m_p denotes the mass, $\boldsymbol{v} = \frac{d\boldsymbol{r}}{dt}$ is the velocity, $\boldsymbol{r}$ is the position vector of the particle, and $\boldsymbol{F}_d$, $\boldsymbol{F}_g$, and $\boldsymbol{F}_{tp}$ represent the drag, the gravity, and the thermophoretic forces, respectively. A virtual mass force is not considered in the present work since it hardly affects the momentum transfer process for in-flight particles [9].

The drag force $\boldsymbol{F}_d$ is usually expressed in terms of fluid velocity $\boldsymbol{u}$ and the time of response τ_p, i.e.

$$\boldsymbol{F}_d = \frac{1}{\tau_p} m_p (\boldsymbol{u} - \boldsymbol{v}). \tag{2}$$

The region of validity of a given drag law depends on the dimensionless relative Reynolds number Re_r of the particles in the flow given by

$$Re_r = \frac{\rho |\boldsymbol{u} - \boldsymbol{v}| d_p}{\mu}, \tag{3}$$

where d_p is the diameter of the particle, and ρ and μ are respectively the mass density and the dynamic viscosity of the fluid. A dimensionless drag coefficient C_D can be introduced to express the time of response as

$$\tau_p = \frac{4\rho_p d_p^2}{3\mu C_D Re_r}. \tag{4}$$

The drag coefficient C_D depends on the relative Reynolds number Re_r and can vary by orders of magnitude during the simulation [25, 27]. For the sake of convenience, C_D is implemented as a piecewise function of Re_r. The data used is given in Table 2 in Appendix A.

The gravity force is written as:

$$\boldsymbol{F}_g = m_p \boldsymbol{g} \frac{(\rho_p - \rho)}{\rho_p}, \tag{5}$$

where ρ_p and ρ are respectively the mass densities of the particle and the surrounding fluid, and $\boldsymbol{g}$ is the gravity vector ($g \approx 9.81 \text{ ms}^{-2}$).

The thermophoretic force accounts for gradients in the temperature T of the fluid and is expressed for continuum flows (Knudsen number $\mathrm{Kn} < < 1$) as:

$$\boldsymbol{F}_{tp} = -\frac{6\pi d_p \mu^2 C_s \Lambda}{\rho(2\Lambda + 1)} \frac{\nabla T}{T}, \tag{6}$$

where μ is the dynamic viscosity of the fluid, $\Lambda = \lambda/\lambda_p$ denotes the ratio of the thermal conductivities of the fluid and the particle, respectively, and $C_s = 1.17$ is a constant parameter. In order to account for a fluid rarefaction, Eq. (6) is modified to read [48]

$$F_{tp} = -\frac{6\pi d_p \mu^2 C_s \left(\Lambda + C_t Kn\right)}{\rho \left(1 + 3C_m Kn\right)\left(1 + 2\Lambda + 2C_t Kn\right)} \frac{\nabla T}{T}, \tag{7}$$

where $C_m = 1.14, C_t = 2.18$.

The heating of the particle by the fluid during its motion is described by the equation of heat balance

$$m_p C_p \frac{dT_p}{dt} = Q_{conv} - Q_r. \tag{8}$$

In Eq. (8), T_p denotes the temperature, C_p is the heat capacity of the particle, Q_{conv} is a heat power accounting for the convective heat transfer between the particle and the fluid, and $-Q_r$ represents the radiative heat loss due to radiative transfer further afield from the particle:

$$Q_{conv} = A_P h_f \left(T - T_p\right), \tag{8a}$$

$$Q_r = A_P \varepsilon_P \sigma_{SB} \left(T_p^4 - T_{amb}^4\right). \tag{8b}$$

In Eqs. (8a) and (8b), A_P is the surface area of the particle, h_f is the convective heat transfer coefficient, ε_P is the particle emissivity, σ_{SB} is the constant of Stefan-Boltzmann, and T_{amb} is the ambient temperature (300 K) [36].

The particle temperature increases due to the heat flux from the hot plasma jet until the melting point of the material is reached. Then, the heat flux is converted to a latent heat of melting L_m or evaporation L_e and the temperature remains constant. In order to account for the phase change (melting or evaporation) of the particle, auxiliary variables $f_{m,e}$ are introduced:

$$m_p L_{m,e} \frac{df_{m,e}}{dt} = Q_{conv} - Q_r. \tag{9}$$

The variables $f_{m,e}$ take values between 0 and 1 corresponding to the former (solid/liq-iud) and the later (liquid/gas) states, respectively.

For values of the temperature T_p beyond the boiling point of the material the particle is made of, the diameter d_p will change due to evaporation according to the following equation

$$\frac{d}{dt}\left(d_p\right) = \frac{2R}{\pi \rho_p d_p^{\,2}}, \tag{10}$$

where $R = -(Q_{conv} - Q_r)/L_e$ is the evaporation rate. The volume of the particle is not spatially resolved so that the temperature T_p has the meaning of the volume temperature of the particle.

Notice that the heat transfer coefficient h_f as defined by the equation [49, 50]

$$h_f = \frac{Nu_p}{d_p} \lambda \tag{11}$$

with Nu_p being the Nusselt number of the particle relates the particle heating with the thermal conductivity of the fluid λ. The dependence $\lambda(T)$ will therefore be chiefly responsible for the effect of fluctuating heating, which the work is focused on.

The description of the particle motion and heating presented so far is applied to a statistically significant number of particles. In the present study this number was taken as 3000. The injection of the particles is specified at the outlet of the injector by a given distribution of particles with respect to their size, a velocity distribution at the injector exit, a randomly chosen position and angle of injection at the injector exit. The particle trajectories are followed until the impact on the substrate placed on the surface DD´. The impingement of molten droplets on the target itself is not considered yet. The velocity and the position of the particle are obtained by integrating Eq. (1), the particle temperature is obtained from Eq. (8), and the melting fraction and the change in the particle diameter are obtained from Eqs. (9) and (10), respectively.

For a better understanding of effects of sprayed particles on the formation of deposition, the K-Sommerfeld number is evaluated in the target plane. The K-Sommerfeld number is expressed as [51]:

$$K = W_e^{1/2} R_e^{1/4}, \tag{12}$$

where W_e and R_e are the Weber and the Reynolds numbers and of impacting particles, respectively:

$$W_e = \frac{\rho_p \cdot d_p \cdot v_n^2}{\sigma_p}, \quad R_e = \frac{\rho_p \cdot d_p \cdot v_n}{\mu_p} \tag{13}$$

In Eq. (13), v_n is the incident normal velocity of the particle, σ_p and μ_p are the surface tension and viscosity of the sprayed particles [52, 53].

Parameters of the Jet Plume

The region of the jet plume (Fig. 1) builds the background in which the motion of the particles occurs. The fluid velocity and temperature are needed for the solution of the Eqs. (1), (8)–(10). These quantities are obtained from the solution of the Navier–Stokes equations for the conservation of mass, momentum, and energy, and a two-equation k-ε turbulence model of the fluid flow in the region ABCDED´C´B´A. It is assumed that the flow is steady and compressible, the plasma is in the state of local thermodynamic equilibrium and optically thin, and the ambient gas is the same as the plasma gas. The inflow of a cold gas through the injector tube is taken into account. The governing equations read.

$$\nabla \cdot (\rho\mathbf{u}) = 0, \tag{14}$$

$$\rho(\mathbf{u} \cdot \nabla)\mathbf{u} = \nabla \cdot \left[-p\boldsymbol{I} + \boldsymbol{K}\right], \tag{15}$$

$$\rho C_{pf}\mathbf{u} \cdot \nabla T + \nabla\boldsymbol{q} = Q_{vd} + Q_p - Q_{rad}, \tag{16}$$

$$\rho(\mathbf{u} \cdot \nabla)k = \nabla \cdot \left[\left(\mu + \frac{\mu_T}{\sigma_k}\right)\nabla k\right] + P_k - \rho\varepsilon, \tag{17}$$

$$\rho(\mathbf{u} \cdot \nabla)\varepsilon = \nabla \cdot \left[\left(\mu + \frac{\mu_T}{\sigma_\varepsilon} \right) \nabla \varepsilon \right] + C_{\varepsilon 1} \frac{\varepsilon}{k} P_k - C_{\varepsilon 2} \rho \frac{\varepsilon^2}{k}. \tag{18}$$

In Eqs. (14)–(18), p denotes the pressure, $\mathbf{I}$ is the identity matrix, $\mathbf{K} = (\mu + \mu_T)(\nabla \mathbf{u} + \nabla \mathbf{u}^T) - \frac{2}{3}(\mu + \mu_T)(\nabla \cdot \mathbf{u})\mathbf{I} - \frac{2}{3}\rho k \mathbf{I}$ is the viscous stress tensor, μ_T is the turbulent viscosity, k represents the turbulent kinetic energy, C_{pf} the heat capacity of the fluid, $\mathbf{q} = -(\lambda + \lambda_T)\nabla T$ is the conductive heat flux with λ and λ_T being respectively the thermal conductivity of the plasma and the turbulent thermal conductivity, Q_{vd} accounts for the viscous dissipation, Q_p is the work for pressure change, Q_{rad} accounts for radiative losses, ε is the turbulent dissipation rate, and $P_k = \mu_T \left[\nabla \mathbf{u} : (\nabla \mathbf{u} + \nabla \mathbf{u}^T) - \frac{2}{3}(\nabla \cdot \mathbf{u})^2 \right] - \frac{2}{3}\rho k \nabla \cdot \mathbf{u}$ is a production term for the turbulent kinetic energy. The turbulent viscosity and thermal conductivity are defined as $\mu_T = \rho C_\mu \frac{k^2}{\varepsilon}$ and $\lambda_T = \frac{\mu_T C_{pf}}{Pr_t}$, respectively. The values of constants used in the standard k-ε model are $C_\mu = 0.09, C_{\varepsilon 1} = 1.44, C_{\varepsilon 2} = 1.92, \sigma_k = 1.0$,$\sigma_\varepsilon = 1.3$, determined from experimental data [54]. The value for the turbulent Prandtl number $Pr_t = 0.3$ is applied in the present study.

Without going into detail, it should be noticed that the turbulence model is important to the modelling of the plasma jet. An overview of different turbulent models is given in [55, 56] among others. The choice of the standard k-ε model in the present work has been made after a validation against published works (see Appendix D). It should be further noticed that the turbulence model enables the account for the effect of turbulent dispersion in the motion of the injected particles [12]. This is included in the drag force (see Eq. (2)) in a way that a random velocity perturbation is added to the mean flow velocity $\mathbf{u}$ based on the local value of the turbulent kinetic energy k [57].

The thermodynamic and transport properties used to obtain the parameters of the plasma jet plume are given in Appendix E for pure argon and mixtures Ar-H_2. In particular, the behavior of the heat conductivity (Fig. 14a), which appears in the heat source Q_{conv} for the injected particles in Eq. (8a), but also in Eqs. (9) and (10), through the heat transfer coefficient h_f (Eq. (11)) is of interest. The admixture of hydrogen to argon leads to an additional peak at a temperature of about 3500 K and a more pronounced peak at a temperature of about 15,000 K in the heat conductivity. Therefore, a spatial fluctuation of the heat source Q_{conv} in the jet plume is expected in mixtures Ar-H_2 even if the temperature distribution behaves monotonically.

The following boundary conditions are applied. At the exit of the plasma torch BB′ (Fig. 1), the values of the temperature, T, and the z-component of velocity, w, are taken from the previously published model of the plasma torch [46], while the radial velocity is set to zero. A turbulence intensity $I_T = 0.16 R_e^{-\frac{1}{8}}$ and a turbulent length scale $L_T = 0.07l$ with l being a characteristic length taken as the diameter of the nozzle exit BB' [58] are set. At the injector exit FG, a given normal velocity and a temperature value of 300 K are set for the cold transversal flow. CD and C′D′ are open boundaries for the temperature and velocity, i.e. zero pressure as well as a zero heat flux or a backflow with a temperature of 300 K are applied. BC and B′C′ are considered as walls, i.e. a non-slip condition and a temperature of 300 K are set. The boundary DD′ is considered as an open boundary for a free jet simulations or a wall when the substrate is included. In the latter case, the temperature of the substrate is set to the value of 450 K that is an experimental estimate.

Results and Discussion

The computation of the particle trajectories and properties in the plasma jet plume of the DC plasma spray torch operated at a current of 600 A in pure argon and in a mixture Ar (40 NLPM)-H_2(14 NLPM) is done for particles made of Al_2O_3. The particle size varies between a few μm and 120 μm (see Fig. 12 in Appendix C). A normal statistical distribution with a mean value of 52.9 μm and standard deviation of 20.5 μm is adopted for the particle sampling. A lower limit of the particle diameter is specified as 5 μm. Each particle is released from a randomly chosen position r on the injector exit of diameter d_{inj} under a randomly chosen polar angle in the range [$-10°$, $10°$]. The particle velocity is expressed as $v_{inj} = (8v_{avg}/7)(1 - 2r/d_{inj})^{1/7}$ [59], where v_{avg} is the average velocity of the carrier gas.

In the computation of the plasma jet in the present work, the inflow of the cold carrier gas (Ar, a flow rate of 3.4 NLPM) is taken into account. Notice that the effect of the carrier flow has been studied in previous works [12, 13, 60]. Njah et al. [60] have shown that mass flow ratio of the main stream and the cold cross flows is the dominant factor that can lead to a deflection of the main flow. Li et al. [12, 13] have considered the effects of cold cross flow in relation to the distance between the edge of plasma jet and the injector exit. Under the conditions in the present work, the plasma jet is hardly influenced by the carrier gas flow.

The computed temperature distribution in the plane CDD´C´ and along the jet axis AE is shown in Fig. 2 in a working gas of pure Ar (a) and Ar-H_2 (b) and Fig. 3a, respectively. The length of the region with temperature values in the range 7000–15,500 K decreases from about 40 mm down to about slightly above 20 mm in the mixture. The decrease of the temperature along the jet axis is steeper in the Ar-H_2 mixture so that in the segment 20–60 mm the temperature in pure argon is higher. However, beyond the axial position z = 70 mm the temperature in the Ar-H_2 mixture slightly rises above the values in pure argon (Fig. 3a). The axial component of the jet velocity in the Ar-H_2 mixture is higher than that in pure argon over the whole distance (Fig. 3b). In particular, at small distances from the torch exit (z = 0), the jet velocity in the Ar-H_2 mixture is well above that in pure argon. This effect might not be obvious since the increase in the flow rate due to the admixture of
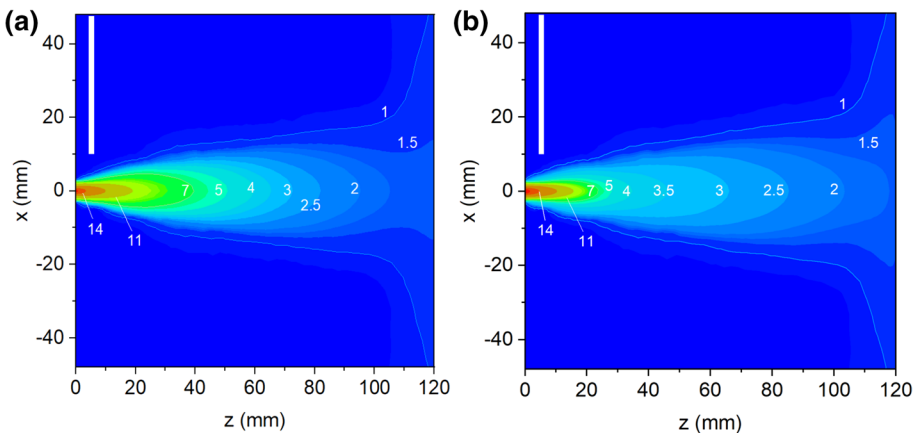
Fig. 2 Temperature distributions (T in 10^3 K) in the symmetry plane of the computational domain CDDC´ of the plasma jet plume in **a** pure Ar and **b** in the mixture Ar-H_2
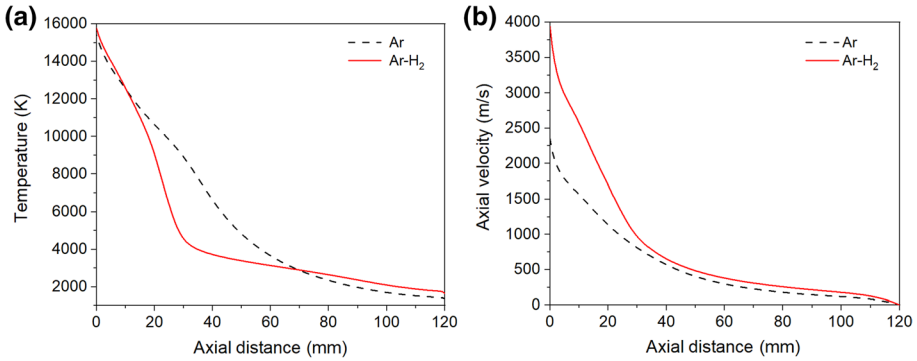
Fig. 3 The plasma jet temperature (**a**) and axial velocity (**b**) along the jet axis in the plume in pure argon (dashed) and in the Ar-H$_2$ mixture (solid)

hydrogen is by a factor of 1.35, whereas the axial jet velocity at the torch exit in the Ar-H$_2$ mixture is by a factor of about 1.7 higher than in pure argon. Furthermore, the dynamic viscosity (Fig. 14c in Appendix E) for pure argon and for the mixture (Ar:H$_2$ = 3:1) is almost the same. The reason lies in the decrease of the mass density in the mixture with hydrogen and the equation of mass continuity (Eq. (14)).

Figures 4 and 5 show the distributions of the thermal conductivity (λ) and the effective thermal conductivity ($\lambda + \lambda_T$) (see section 'Parameters of the jet plume') in the symmetry plane of the computational domain CDD'C', respectively, for pure argon (a) and for the mixture Ar-H$_2$. Notice the different scales in the graphs. The turbulent thermal conductivity λ_T introduced by the turbulent flow can be by about one or two orders of magnitude larger than λ. Indeed, according to the definition, the combined effects of turbulent viscosity μ_T and gas specific heat C_{pf} largely increase λ_T in the temperature region, where dissociation of the molecular gas occurs. As a matter of fact, the peak value of the effective thermal conductivity of the mixture Ar-H$_2$ tends to approach the value of 140 Wm^{-1} K^{-1} in the region of the plasma jet 40 mm < z < 55 mm and is almost by a factor of 9 larger than that in pure Ar. The effective thermal conductivity (Fig. 5a, b) affects the density of
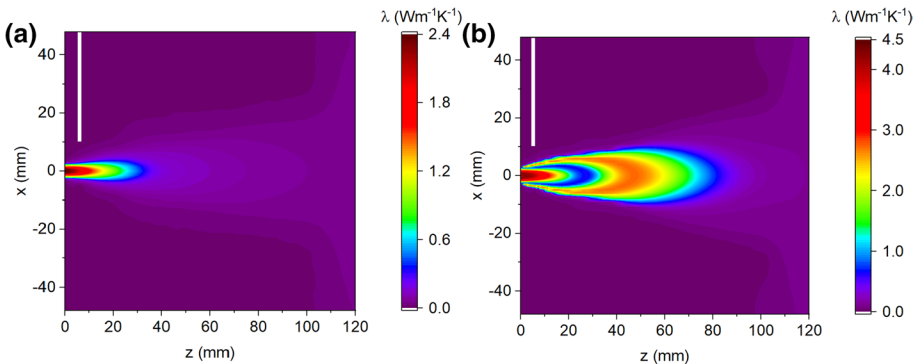
Fig. 4 Distribution of the thermal conductivity λ in the symmetry plane of the computational domain CDDC´ for pure Ar (**a**) and mixture Ar-H$_2$ (**b**)
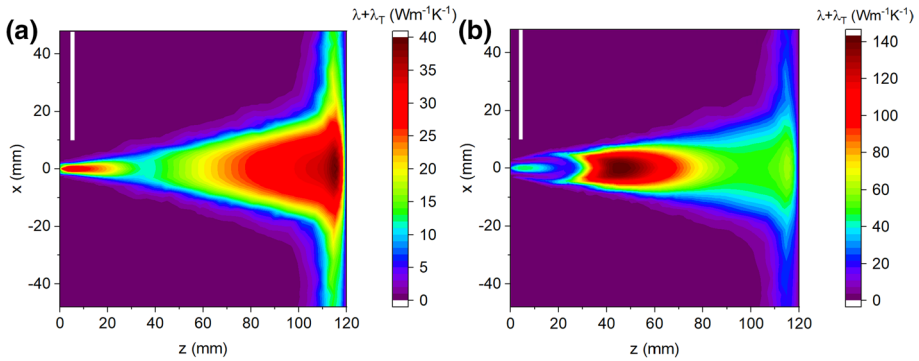
Fig. 5 Distribution of the effective thermal conductivity $\lambda + \lambda_T$ in the symmetry plane of the computational domain CDD′C′ for pure Ar (**a**) and mixture Ar-H$_2$ (**b**)

the conductive heat flux **q** in Eq. (16), from which the temperature of the plasma jet is obtained. The thermal conductivity in the Ar-H$_2$ mixture remains well above that in pure argon for distances z > 30 mm. This explains the lower temperature values in the gas mixture shown in Fig. 3a.

As shown in Fig. 4a, b, not only differ the values of the thermal conductivity in the hot region of the plasma jet by almost a factor of two, but the thermal conductivity in the Ar-H$_2$ mixture remains well above that in pure argon for distances z > 30 mm and implies a second peak, which is not observed in pure argon. As mentioned above, the heating of the particles injected in the plasma jet depends on the thermal conductivity of the fluid λ. Therefore, the particles will undergo a fluctuating heating in the mixture Ar-H$_2$ that is not the case in pure argon. This is expected to have an impact on the particle behavior and parameters.

Figure 6a shows the temperature of the plasma jet (T) and Fig. 6b shows the heat source (Q_{conv}) as a function of the distance z for two selected particles identified by numbers P658 and P678 as injected in the mixture Ar-H$_2$ and in pure argon. The diameters of the particles are 19.97 μm and 37 μm for P658 and P678, respectively. Depending on the particle trajectory, the values of T and Q_{conv} at the same axial distance can differ. After being released at the injector exit, the particles cross the cold jet periphery and enter the hot region of the jet with temperatures above 10,000 K. The larger (and heavier) particle (P678) penetrates closer to the jet axis, where the jet temperature is higher. The jet temperatures attributed to the particles for z between 20 and 60 mm are higher in pure Ar than in the Ar-H$_2$ mixture, in agreement with the results in Fig. 3a.

As discussed above, the thermal conductivity of the plasma jet λ has a well pronounced spatially fluctuating behavior in the mixture Ar-H$_2$ (Fig. 4b) and this affects the heat source Q_{conv} acting on the particles (Fig. 6b). Notice that the power loss due to radiation ($-Q_r$) shown in (Fig. 6c) is weaker by 2–3 orders of magnitude than Q_{conv} under the conditions of the present study. While the heat source in pure Ar first increases as the particles penetrate the jet and then monotonically decreases, the heat source acting on the particles in the Ar-H$_2$ mixture is characterized by a number of peaks. A very narrow peak can be seen at $z \sim 7$ mm (see the zoomed-in graph Fig. 6b) since particles cross over the thin band with increased values of λ close to the position of the injector exit (Fig. 4b). The second peak corresponds to the particle motion in the hot region
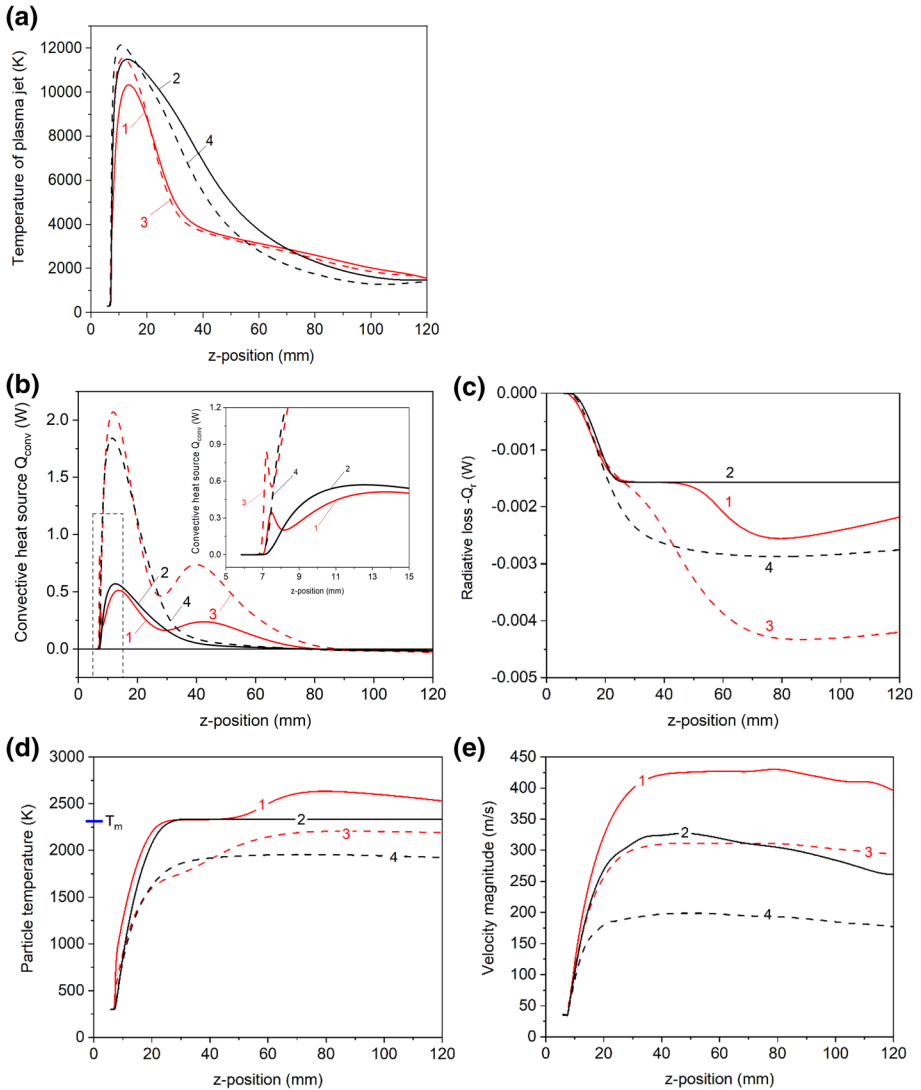
Fig. 6 Quantities attributed to the selected particles: **a** the temperature of the plasma jet, **b** the convective heat source and **c** the radiative heat loss, **d** the computed particle temperature, and **e** the velocity magnitude of the selected particles in the plasma jet generated in the mixture Ar-H$_2$ and in pure Ar. Curve notations: 1—P658 in Ar-H$_2$; 2—P658 in Ar; 3—P678 in Ar-H$_2$; 4—P678 in Ar

of the plasma jet (10 mm $< z <$ 20 mm). The third peak occurs in the downstream jet (30 mm $< z <$ 70 mm), where λ exhibits a broaden enhancement. Notice that the peaks are stronger pronounced and shifted to the lower z-positions for the larger and heavier particle P678. The first effect can be related to the larger surface of the particle A_P appearing in Q_{conv} given by Eq. (8a). The second effect indicates that larger particles cross over the region of enhanced λ at radial positions x $<$ 0, which are farther away from the jet axis than for smaller particles (Fig. 4b).

The development of the particle temperature and velocity during the motion in the plasma jet is shown respectively in Fig. 6d and e. The temperature of P658 increases rapidly and reaches the melting point T_m (2327 K) at z-positions between 20 and 30 mm in both Ar-H_2 (curve 1) and pure Ar (curve 2). The temperature of P678 remains below the T_m-value in both gases (curves 3 and 4) even though the heat source of P678 is larger by a factor of about four than that for P658 at $z \sim 15$ mm. Notice that the increase in the particle diameter by a factor of two leads to an increase in the particle surface A_p by a factor of four and to an increase in the particle mass m_p by a factor of eight.

Once the temperature T_m is reached, the particle temperature remains constant up to $z \sim$ 45 mm (curves 1 and 2 in Fig. 6d). Beyond this z-position, P658 is exposed to the next enhancement of the heat source in the mixture Ar-H_2, the molten fraction approaches the value of one, and the temperature further increases and stays well above T_m even in the range $z > 80$ mm, where the convective heat source is turning its sign (Fig. 6b) since T_p becomes higher than T. As a result, the particle is repeatedly heated by the plasma jet generated in the mixture Ar-H_2 in contrast to the case of pure argon.

Once the particle is injected into the plasma jet and approaches the hot region, its velocity first increases (Fig. 6e) due to the high jet velocity and the positive drag force (see Eq. (2), the contribution of the other forces is much lower). The jet velocity in the mixture Ar-H_2 (Fig. 3b) is larger and as a result, the particle velocity in the mixture is larger than in Ar. The less inert smaller particles reach larger velocities than the larger ones (compare curves 1 and 3 with curves 2 and 4 in Fig. 6e). Downstream the jet, the jet velocity decreases and the drag force changes the sign. This leads to the decrease of the particle velocity for $z > 50$ mm. The effect of the turbulent dispersion can be seen in both gases for P658 (small fluctuations in curves 1 and 2), while it is negligible for P678.

A total number of 3000 particles has been found to be statistically significant in the present study. In general, already a computation with 1000 particles has enabled representative results. The increase in the number to 5000 has increased the computational time without changing the results substantially. Figure 7 presents the particle trajectories in the
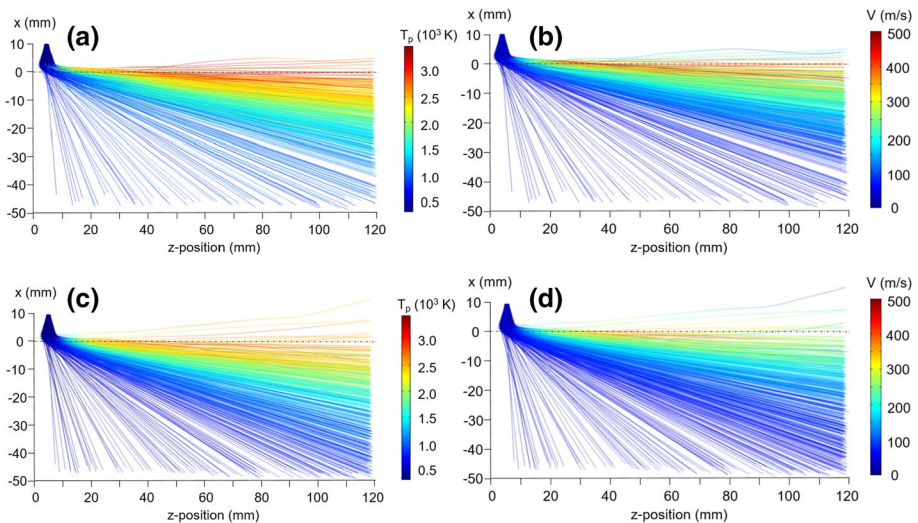

Fig. 7 The thermal (**a, c**) and velocity history (**b, d**) in different background gases: Ar-H_2 (**a, b**) and Ar (**c, d**). Notice that for the sake of readability, 20% of the trajectories are presented

color scale of the particle temperature T_p (a,c), and in the color scale of the particle velocity v (b,d) for a number of injected particles in the plasma jet in Ar (a, b) and in Ar-H_2 (c, d) in the plane CDD´C´. The results indicate that particles processed in the Ar-H_2 mixture become hotter and faster during their motion towards the substrate. In particular, small particles (say d_p up to 20 µm) are stronger heated since their trajectories stay closer to the jet axis. Large particles (say $d_p > 80$ µm) tend to leave the computational domain without reaching the substrate. The trajectories in the region above the torch axis (x > 0) that correspond to small particles ($d_p < 20$ µm) are somewhat deformed due to effect of turbulent dispersion leading to a random movement of particles. The peak values of particle temperature between 2700 and 3200 K and the velocity between 400 ms^{-1} and 500 ms^{-1} are reached not in the vicinity of the substrate but at $z \sim 60$ mm due to the decrease in the jet temperature and axial velocity. These values are in a good agreement with experimental findings in Fig. 8 that are obtained by monitoring during operation time of 40 h with the Tecnar Accuraspray-g3c system [61]. This system provides an accurate and reliable observation of the spray plume. The data is collected on a real-time basis and undergoes a computer processing that enables both a real-time and an offline analysis.

Figures 9 and 10 show the parameters of the particles on the x–y plane of the substrate. For the particles injected into the Ar-H_2 mixture and reaching the substrate at $z = 12$ cm, particle temperatures T_p between 2700 and 3250 K (Fig. 9a) and particle velocities between 350 ms^{-1} and 450 ms^{-1} (Fig. 9b) are most strongly represented for positions -5 mm < x,y < 5 mm. The corresponding values in pure Ar are lower and represented by less particles (Fig. 9c, d). Notice that in Ar-H_2 mixture, the jet velocity is larger by about a factor of two than in pure Ar for axial positions 5 mm < z < 20 mm (see Fig. 3b). The center of the injector is at axial position z = 6 mm so that the particles injected into the Ar-H_2 mixture are exposed to a faster jet flow than in pure Ar. Therefore, they are able to move longer close to the jet axis and the particles trajectories are less inclined with respect to the jet axis (see Fig. 7). This effect becomes well pronounced in the comparison of the distributions on Figs. 9a, b and 10a, b with those in Figs. 9c, d and 10c, d. In Figs. 9a, b and 10a, b, the area, corresponding to positions – 50 mm < x < 30 mm and –10 mm < y < 10 mm are rarely occupied. In particular, larger particles become likely less deflected in Ar-H_2 in comparison with those in Ar (Fig. 10a, c).

The distribution of the K-Sommerfeld number on substrate plane before formation of coatings as evaluated by Eq. (12) is shown in Fig. 10 b, d. In case of pure Ar,

Fig. 8 The particle temperature and velocity obtained by monitoring with the Tecnar Accuraspray-g3c system. The measurement points are collected during operation time of 40 h
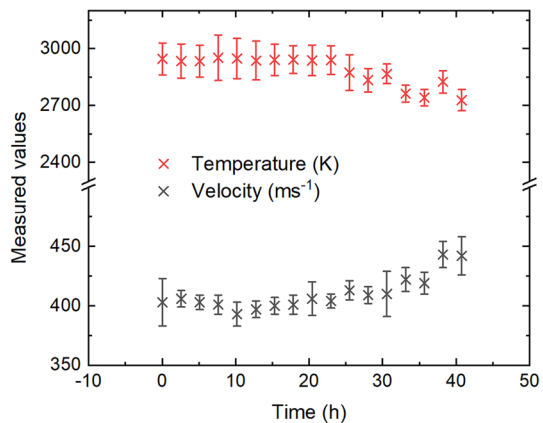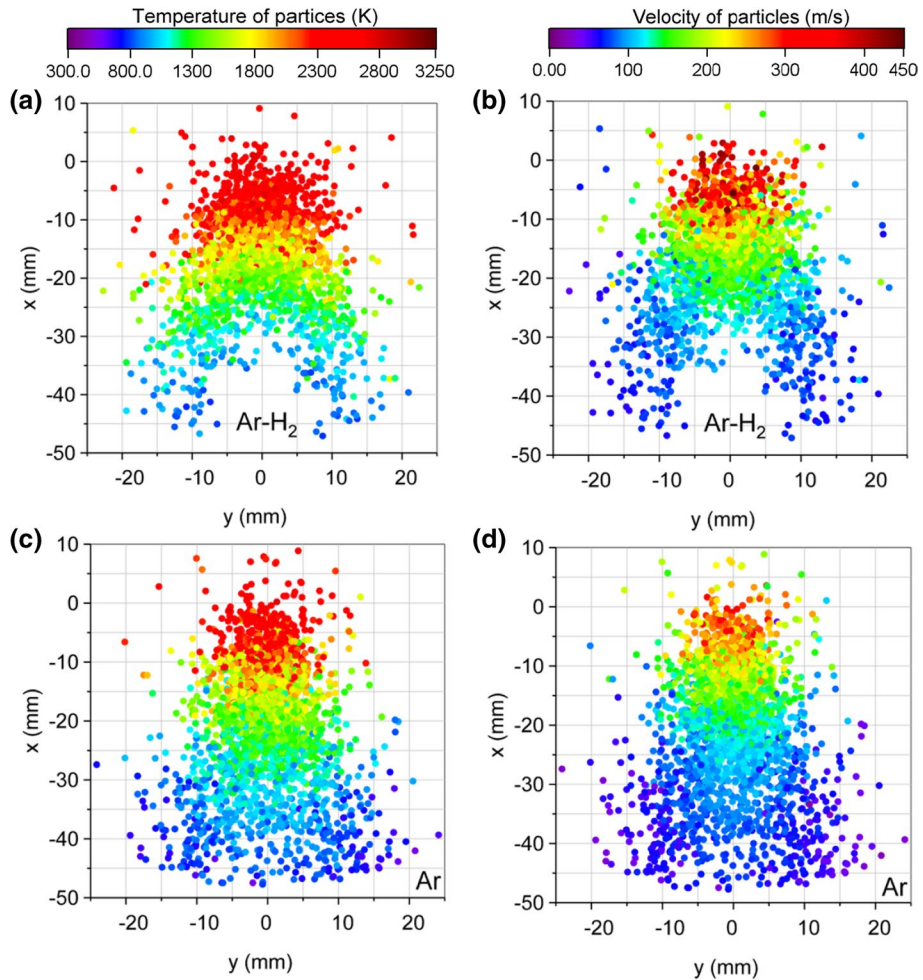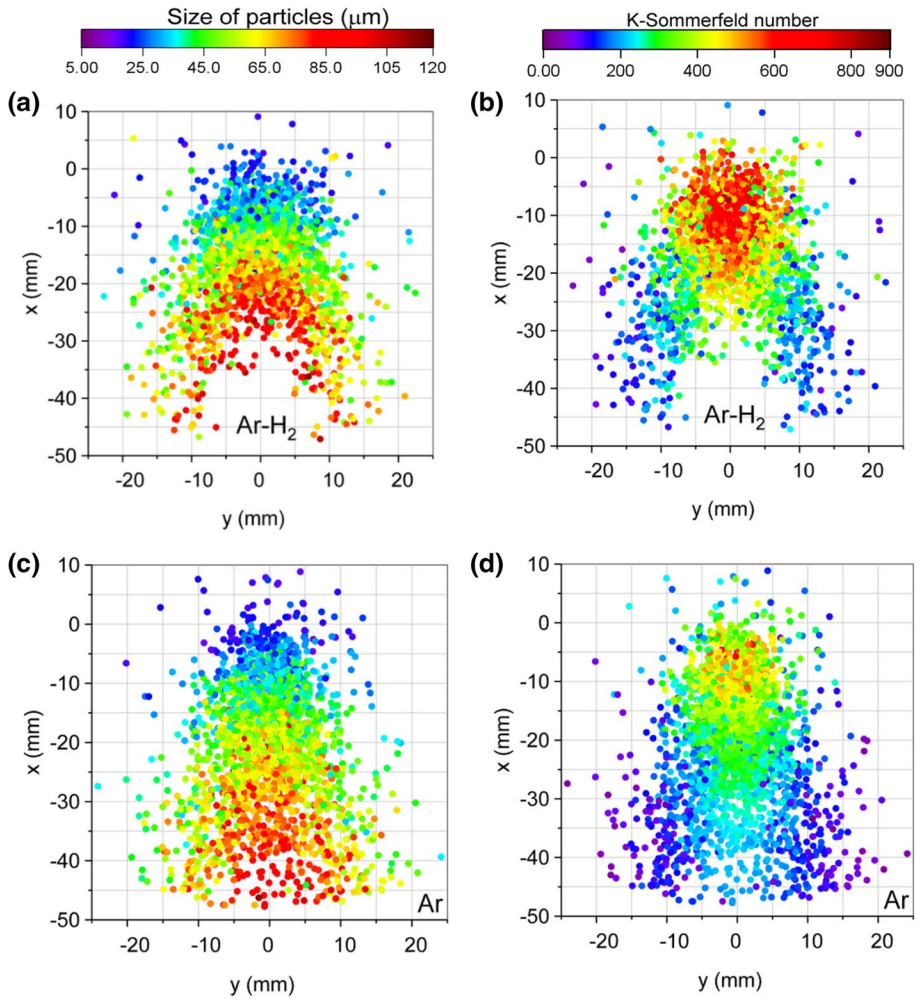
Fig. 9 Particle temperature (**a, c**) and velocity (**b, d**) on the substrate plane ($z = 12$ cm) for particles injected in the Ar-H$_2$ mixture (**a, b**) and in pure Ar (**c, d**)

the K-Sommerfeld number is well below than that in the Ar-H$_2$ mixture. According to the accepted classification [7, 8, 51], $K < 3$ corresponds to a rebound, $3 < K < 57.7$ – to a deposition, and $K > 57.7$ – to a deposition with splashing. The splashing effect is typical for high flow rates.

A summary of some parameters of the tracing of Al$_2$O$_3$ particles injected into the plasma jets operating in pure Ar and in the Ar-H$_2$ mixture is given in Table 1. The particle tracing model predicts a higher number of particles reaching the substrate, and a higher number of evaporated and molten particles for the plasma spraying in Ar-H$_2$ than in pure Ar. As a result of the fluctuating heating that occurs in the mixture Ar-H$_2$, higher average temperatures of the particles can be reached. The average flight times in the Ar-H$_2$ mixture are shorter than in pure Ar due to the higher corresponding velocities reached.

The data that supports the results of this study are openly available in INPTDAT, reference number [62].

Fig. 10 Particle diameter (**a, c**) and K-Sommerfeld number (**b, d**) on the substrate plane ($z = 120$ mm) for particles injected in the Ar-H$_2$ mixture (**a, b**) and in pure Ar (**c, d**)

Table 1 Statistics on the tracing of Al$_2$O$_3$ particles injected into a plasma jet in Ar and in Ar-H$_2$

	Ar	Ar-H$_2$
Total number	3000	3000
Particles reaching the substrate	2320 (77.3%)	2578 (85.9%)
Evaporated	51 (1.7%)	89 (2.9%)
Molten	268 (8.9%)	492 (16.4%)
Average parameters of the particles reaching the substrate		
Velocity (ms^{-1})	141.1	190.0
Temperature (K)	1502.8	1781.5
K-number	285.5	457.8
Flight time (ms)	1.25	1.03

Conclusion

The present work continues the plasma spraying related studies that have started with a model of the plasma spray torch Oerlikon Metco F4MB-XL [46]. Here, a particle tracing model along with a turbulent model of the plasma jet in the plume region of a plasma spray torch are employed. The study considers the effect of a fluctuating heating of Al_2O_3 particles that are injected into a plasma jet generated in a mixture of Ar (40 NLPM) and H_2 (14 NLPM) with respect to the heating process in pure Ar. The model is set as three-dimensional in order to account for the side-on particle injection and validated against published data. The plasma spray torch is operated with a DC current of 600 A. The size of injected particles varies in the range (5–120) μm. The results can be summarized as follows.

The presence of the molecular gas (H_2) leads to a higher jet velocity, in particular at small distances from the torch exit, and a steeper decrease of the plasma temperature in the region z = (20–60) mm in comparison to pure Ar. The temperature decrease is caused by the large increase in the effective thermal conductivity of the mixture Ar-H_2.

The heating of the injected particles is dominated by the convective heat transfer between the particles and the fluid. The radiative heat loss is of minor importance. The convective heat source exhibits a well pronounced spatially fluctuating structure due to the enhancement of the thermal conductivity resulting from dissociation and ionization in temperature range of 2500–4000 K and 13,000–14,000 K, respectively. The injected particles travel towards the substrate through the heat source field crossing a very narrow peak ($z \sim 7$ mm) close to the position of the injector exit, then a second peak corresponding to the hot region of the plasma jet (10 mm < z < 20 mm), and a third peak in the downstream jet (30 mm < z < 70 mm). The peaks are stronger pronounced and shifted closer to the torch exit for larger and heavier particles. As a result, the temperature of particles of equal properties can increase rapidly and reach the melting point T_m in both Ar-H_2 and pure Ar, but only in the mixture Ar-H_2 the particle is repeatedly heated and its temperature can further increase. Particles injected in the gas mixture reach the substrate with a higher average temperature and velocity.

Forthcoming works will focus on the simulation of the particle impingement on the substrate and the process of the coating formation.

Appendix

Supplementary data used in the models developed are given in this section.

Appendix A: Drag coefficient

Table 2 summarizes the expressions for the drag coefficient applied in Eq. (4) according the data in [25, 27].

**Table 2** Expressions of the drag coefficient as a piecewise function of the relative Reynolds number

Range of Re_r	Correlation of C_D
$Re_r \leq 0.01$	$C_D = \frac{24}{Re_r}(1 + \frac{3}{16}Re_r)$
$0.01 < Re_r \leq 20$	$C_D = \frac{24}{Re_r}(1 + 0.1315Re_r^{0.82-0.05w})$
$20 < Re_r \leq 260$	$C_D = \frac{24}{Re_r}(1 + 0.1935Re_r^{0.6305})$
$260 < Re_r \leq 1500$	$\log C_D = 1.6435 - 1.1242w + 1.558w^2$
$1500 < Re_r \leq 12000$	$\log C_D = -2.4571 + 2.5558w - 0.9295w^2 + 0.1049w^3$
$12000 < Re_r \leq 44000$	$\log C_D = -1.9181 + 0.6370w - 0.0636w^2$
$44000 < Re_r \leq 3.38 \times 10^5$	$\log C_D = -4.3390 + 1.5809w - 0.1546w^2$
$3.38 \times 10^5 < Re_r \leq 4 \times 10^5$	$C_D = 29.78 - 5.3w$
$4 \times 10^5 < Re_r \leq 1 \times 10^6$	$C_D = 0.1w - 0.49$
$10^6 < Re_r$	$C_D = 0.19 - 8 \times 10^4/Re_r$

Remark: $w = \log Re_r$ and log is the base 10 logarithm

Appendix B: Validation of the particle tracing model

In order to validate the computational model for the particle tracing described in section 'Motion of the injected particles', computations were performed for four kinds of particles (Al$_2$O$_3$, Fe, dense and porous ZrO$_2$). The properties of the injected particles are taken from published data [7]. The particles are injected into the plasma jet with a uniform diameter of 35 μm and a velocity of 20 ms^{-1}. The center of the injector is 6 mm away from the torch exit and 8 mm away from the torch axis. The computed trajectories, velocities and temperatures for the corresponding particles are shown in Fig. 11 (a)-(c). The good quantitative agreement with the results by Djebali et al. [7] demonstrates the validity of the particle tracing model in the present work. Certain deviations exist in the particle temperatures for dense ZrO$_2$ particles. Since the particle heating is closely related to the temperature of the plasma jet, the deviations can be associated with the deviations shown in Fig. 13.

Fig. 11 Parameters of the particles along the distance z: **a** trajectory (radial position), **b** velocity, and **c** temperature obtained in the present work (solid curves) and in a published work by Djebali et al. [7] (symbols)
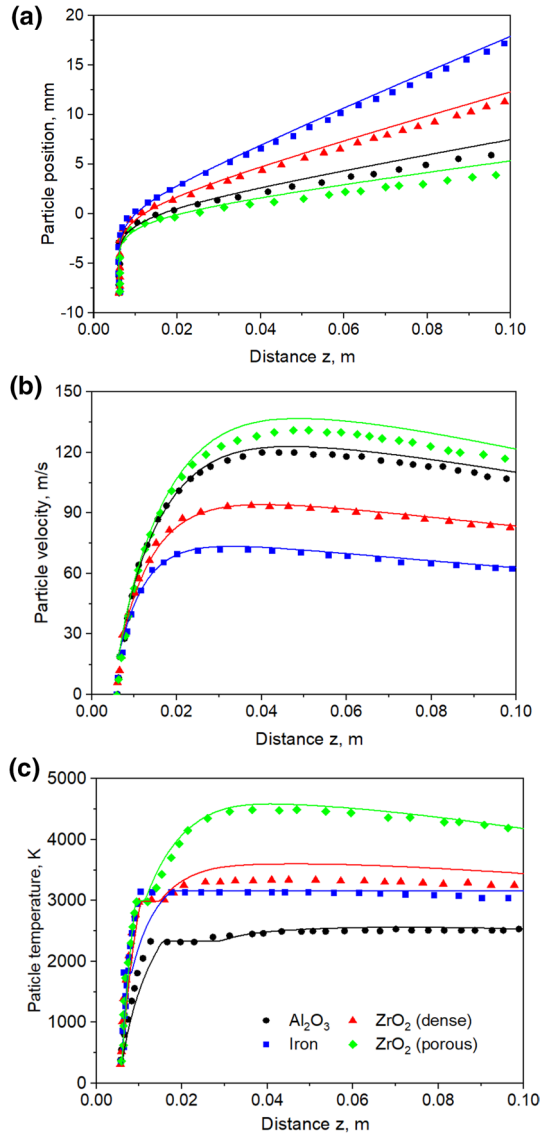
Appendix C: Particle size distribution

The particle size distribution is measured based on the static light scattering (SLS) technique combined with a Mie scattering model. The SLS experiment was performed employing the Mastersizer 2000 device [63]. The results obtained for the Al_2O_3 powder used in the plasma spray experiments is shown in Fig. 12. A normal distribution with mean value of 52.9 μm and standard deviation of 20.5 μm is derived for the use in the tracing model.

Fig. 12 Particle size distribution applied in the model of particle tracing
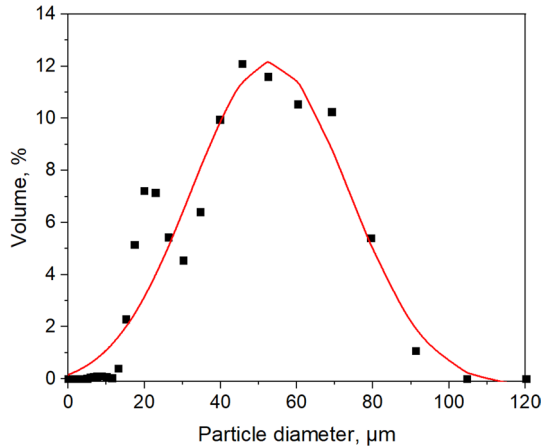
## Appendix D: Validation of the turbulent jet model

The model of the turbulent jet in the plume region is validated against experimental and simulation works [7, 64–69]. For that purpose, the torch exit BB′ was taken with a radius AB = R = 4 mm, a distance AE = 100 mm, and a radial extend BC = 44 mm. The model is two-dimensional and axisymmetric with AE being the axis of symmetry. The conditions for the plasma temperature and velocity on AB are therefore expressed as follows:

$$T = \left(T_{max} - T_0\right)\left(1 - \left(\frac{r}{R}\right)^4\right) + T_0, v = v_{max}\left(1 - \left(\frac{r}{R}\right)^2\right),$$

where $T_{max} = 13500 K$, $v_{max} = 520 m/s$, and $T_0 = 300$ K [64–66].

We notice that for the sake of validation, the boundary condition on ED is set as "open boundary" instead of "wall". This does not affect the results of the fluid flow in the core region of the plasma jet.

The comparison with published data for the plasma temperature Fig. 13a and the plasma velocity Fig. 13b along the jet axis z (AE) (see Fig. 1) shows a fair agreement. The plasma velocity predicted by Djebali et al. [66] is the largest in the downstream region, while the temperature predicted by Zhang et al. [65] is the lowest. The results in the present work agree well with experimental and simulation works by Pfender et al. [64, 68].
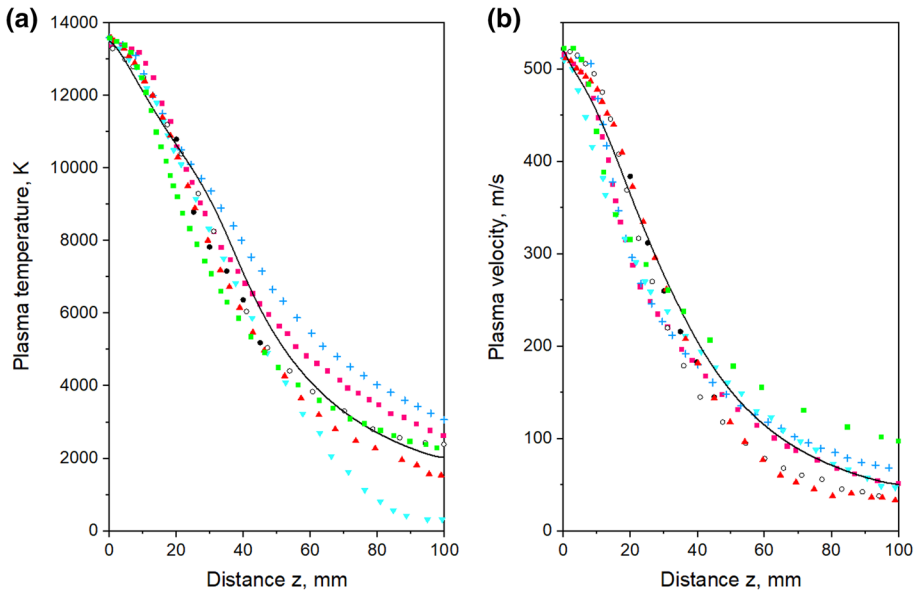
Fig. 13 Axial distribution of the plasma temperature (**a**) and the plasma velocity (**b**): solid line (present work), solid squares (R. Djebali 7, 66), solid circles (experiment E. Pfender 64, 68), open circles (simulation E. Pfender 64, 68), cross symbol (Jets&Podres 67), solid down trinangle (H. Zhang 65), solid up triangle (Y. Z. Sun 69)

Appendix E: Thermodynamic and transport properties and net emission coefficient of the plasma

The thermodynamic and transport properties used in the model of the plasma jet in the plume region are shown in Fig. 14. The transport properties are computed applying the Chapman-Enskog method. The computed values are compared with published data in [45]. The net emission coefficient of the plasma is taken from published works [70, 71].
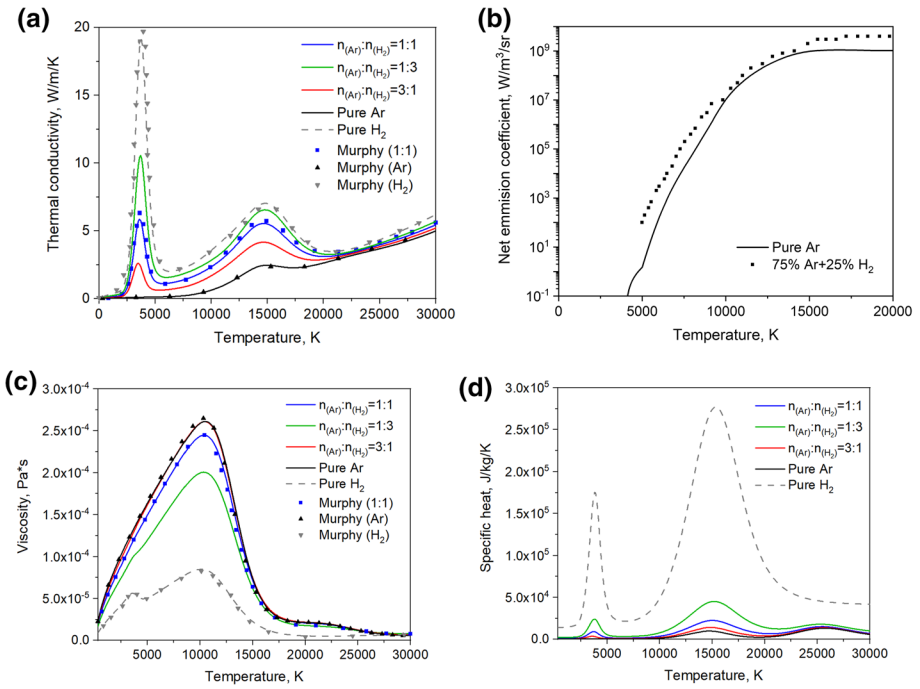
Fig. 14 Thermal conductivity (**a**), net emission coefficient (**b**), viscosity (**c**) and specific heat C$_p$ (**d**) of pure argon and mixtures of argon with hydrogen

References

1. Vardelle A, Moreau C, Themelis NJ, Chazelas C (2015) A perspective on plasma spray technology. Plasma Chem Plasma Process 35:491–509. https://doi.org/10.1016/j.surfcoat.2020.125731
2. Chazelas C, Trelles JP, Vardelle A (2017) The main issues to address in modeling plasma spray torch operation. J Therm Spray Technol 26:3–11. https://doi.org/10.1007/s11666-016-0500-y

3. Fauchais P, Heberlein JVR, Boulos M (2014) Thermal spray fundamentals: from powder to part. Springer, New York

4. Zhukovskii R, Chazelas C, Rat V, Vardelle A, Molz R (2021) Predicted anode arc attachment by LTE (local thermodynamic equilibrium) and 2-T (two-temperature) arc models in a cascaded-anode DC plasma spray torch. J Therm Spray Technol 31:28–45. https://doi.org/10.1007/s11666-021-01253-4

5. Trelles JP, Heberlein JVR, Pfender E (2007) Non-equilibrium modelling of arc plasma torches. J Phys D: Appl Phys 40:5937–5952. https://doi.org/10.1088/0022-3727/40/19/024

6. Trelles JP (2013) Computational study of flow dynamics from a dc arc plasma jet. J Phys D: Appl Phys 46:255201. https://doi.org/10.1088/0022-3727/46/25/255201

7. Djebali R, ElGanaoui M, Jaouabi A, Pateyron B (2016) Scrutiny of spray jet and impact characteristics under dispersion effects of powder injection parameters in APS process. Int J Therm Sci 100:229–239. https://doi.org/10.1016/j.ijthermalsci.2015.09.027

8. Djebali R (2017) Optimization study of the operating conditions to improve the quality of surfaces coating obtained by plasma spraying process. J Therm Eng 3:1411–1418. https://doi.org/10.18186/journal-of-thermal-engineering.330186

9. Bobzin K, Öte M (2017) Modeling plasma–particle interaction in multi-arc plasma spraying. J Therm Spray Technol 26:279–291. https://doi.org/10.1007/s11666-016-0514-5

10. Bobzin K, Öte M, Schein J, Zimmermann S (2017) Numerical study on plasma jet and particle behavior in multi-arc plasma spraying. J Therm Spray Technol 26:811–830. https://doi.org/10.1007/s11666-017-0564-3

11. Bobzin K, Heinemann H, O'Brien A (2022) Capturing the influence of jet fluctuations on particles in plasma spraying. J Therm Spray Technol 31:59–69. https://doi.org/10.1007/s11666-021-01307-7

12. Li HP, Chen X (2002) Three-dimensional modeling of the turbulent plasma jet impinging upon a flat plate and with transverse particle and carrier-gas injection. Plasma Chem Plasma Process 22:27–58. https://doi.org/10.1023/A:1012988430995

13. Li HP, Pfender E (2007) Three dimensional modeling of the plasma spray process. J Therm Spray Technol 16:245–260. https://doi.org/10.1007/s11666-007-9023-x

14. Coudert JF, Planche MP, Fauchais P (1995) Characterization of dc plasma torch voltage fluctuations. Plasma Chem Plasma Process 16:S211–S227. https://doi.org/10.1007/BF01512636

15. Nemchinsky V (2012) Cathode erosion in a high-pressure high-current arc: calculations for tungsten cathode in a free-burning argon arc. J Phys D: Appl Phys 45:135201. https://doi.org/10.1088/0022-3727/45/13/135201

16. Konishi K, Tanaka M, Shigeta M, Ishida K (2017) Numerical analysis of dynamic behavior of additives in electrode during TIG welding process. Q J Jpn Weld Soc 35:73–84. https://doi.org/10.2207/qjjws.35.73

17. Baeva M, Benilov MS, Zhu T, Testrich H, Kewitz T, Foest R (2022) Modelling and experimental evidence of the cathode erosion in a plasma spray torch. J Phys D: Appl Physics 5:365202. https://doi.org/10.1088/1361-6463/ac791c

18. Modirkhazeni SM, Trelles JP (2018) Non-transferred arc torch simulation by a non-equilibrium plasma laminar-to-turbulent flow model. J Therm Spray Technol 27:1447–1464. https://doi.org/10.1007/s11666-018-0765-4

19. Zhukovskii R, Chazelas C, Vardelle A, Rat V (2020) Control of the arc motion in DC plasma spray torch with a cascaded anode. J Therm Spray Technol 29:3–12. https://doi.org/10.1007/s11666-019-00969-8

20. Zhukovskii R, Chazelas C, Vardelle A, Rat V, Distler B (2020) Effect of electromagnetic boundary conditions on reliability of plasma torch models. J Therm Spray Technol 29:894–907. https://doi.org/10.1007/s11666-020-01052-3

21. Bobzin K, Öte M, Knoch MA, Alkhasli I (2019) Macroscopic particle modeling in air plasma spraying. Surf Coat Technol 364:449–456. https://doi.org/10.1016/j.surfcoat.2018.07.056

22. Djebali R, Pateyron B, El Ganaoui M (2013) A lattice Boltzmann based investigation of powder in-flight characteristics during APS process, part II: Effects of parameter dispersions at powder injection. Surf Coat Technol 220:157–163. https://doi.org/10.1016/j.surfcoat.2013.01.001

23. Bobzin K, Wietheger W, Heinemann H, Dokhanchi SR, Rom M, Visconti G (2021) Prediction of particle properties in plasma spraying based on machine learning. J Therm Spray Technol 30:1751–1764. https://doi.org/10.1007/s11666-021-01239-2

24. Zhu JW, Wang X, Kou L, Zheng L, Zhang H (2020) Prediction of control parameters corresponding to in-flight particles in atmospheric plasma spray employing convolutional neural networks. Surf Coat Technol 394:125862. https://doi.org/10.1016/j.surfcoat.2020.125862

25. Vardelle M, Vardelle A, Fauchais P, Boulos MI (1983) Plasma-particle momentum and heat transfer: Modelling and measurements. AIChE J 29:236–243. https://doi.org/10.1002/aic.690290210

26. Vardelle M, Vardelle A, Fauchais P (1993) Spray parameters and particle behavior relationships during plasma spraying. J Therm Spray Technol 2:79–91. https://doi.org/10.1007/BF02647426

27. Zhang T, Gawne DT, Liu B (2000) Computer modelling of the influence of process parameters on the heating and acceleration of particles during plasma spraying. Surf Coat Technol 132:233–243. https://doi.org/10.1016/S0257-8972(00)00847-1

28. Das DK, Sivakumar R (1990) Modelling of the temperature and the velocity of ceramic powder particles in a plasma flame - I. Alumina Acta Metall Mater 38:2187–2192. https://doi.org/10.1016/0956-7151(90)90086-V

29. Dyshlovenko S, Pateyron B, Pawlowski L, Murano D (2004) Numerical simulation of hydroxyapatite powder behaviour in plasma jet. Surf Coat Technol 179:110–117. https://doi.org/10.1016/S0257-8972(03)00799-0

30. Gawne DT, Liu B, Bao Y, Zhang T (2005) Modelling of plasma-particle two-phase flow using statistical techniques. Surf Coat Technol 191:242–254. https://doi.org/10.1016/j.surfcoat.2004.02.032

31. Ko TH, Chen HK (2005) Three-dimensional isothermal solid-gas flow and deposition process in a plasma spray torch with solid shield: A numerical study. Surf Coat Technol 200:2152–2164. https://doi.org/10.1016/j.surfcoat.2004.06.036

32. Mostaghimi J, Chandra S, Ghafouri-Azar R, Dolatabadi A (2003) Modeling thermal spray coating processes: a powerful tool in design and optimization. Surf Coat Technol 163:1–11. https://doi.org/10.1016/S0257-8972(02)00686-2

33. Fauchais P (2004) Understanding plasma spraying. J Phys D: Appl Physics 37:R86. https://doi.org/10.1088/0022-3727/37/9/R02

34. Planche MP, Bolot R, Coddet C (2003) In-flight characteristics of plasma sprayed alumina particles: measurements, modeling, and comparison. J Therm Spray Technol 12:101–111. https://doi.org/10.1361/105996303770348555

35. Thiyagarajan TK, Sreekumar KP, Selvan V, Ramachandran K, Ananthapadmanabhan PV (2010) Simulation studies to optimize the process of plasma spray deposition of yttrium oxide. J Phys: Conf Ser 208:012116. https://doi.org/10.1088/1742-6596/208/1/012116

36. Wan YP, Prasad V, Wang GX, Sampath S, Fincke JR (1999) Model and powder particle heating, melting, resolidification, and evaporation in plasma spraying processes. J Heat Transfer 121:691–699. https://doi.org/10.1115/1.2826034

37. Wan YP, Fincke JR, Sampath S, Prasad V, Herman H (2002) Modeling and experimental observation of evaporation from oxidizing molybdenum particles entrained in a thermal plasma jet. Int J Heat Mass Transf 45:1007–1015. https://doi.org/10.1016/S0017-9310(01)00214-9

38. Wei DY, Farouk B, Apelian D (1988) Melting metal powder particles in an inductively coupled RF plasma torch. Metall Mater Trans B 19:213–226. https://doi.org/10.1007/BF02654205

39. Westhoff R, Trapaga G, Szekely J (1992) Plasma-particle interactions in plasma spraying systems. Metall Mater Trans B 23:683–693. https://doi.org/10.1007/BF02656448

40. Xu DY, Wu XC, Chen X (2003) Motion and heating of non-spherical particles in a plasma jet. Surf Coat Technol 171:149–156. https://doi.org/10.1016/S0257-8972(03)00259-7

41. Zhang T, Bao Y, Gawne DT, Liu B, Karwattzki J (2006) Computer model to simulate the random behaviour of particles in a thermal-spray jet. Surf Coat Technol 201:3552–3563. https://doi.org/10.1016/j.surfcoat.2006.08.108

42. Meillot E, Balmigere G (2008) Plasma spraying modeling: particle injection in a time fluctuating plasma jet. Surf Coat Technol 202:4465–4469. https://doi.org/10.1016/j.surfcoat.2008.04.028

43. Djebali R, Pateyron B, El Ganaoui M (2015) Scrutiny of plasma spraying complexities with case study on the optimized conditions toward coating process control. Case Stud Therm Eng 6:171–181. https://doi.org/10.1016/j.csite.2015.09.005

44. Pfender E, Lee YC (1985) Particle dynamics and particle heat and mass transfer in thermal plasmas. Part I. The motion of a single particle without thermal effects. Plasma Chem Plasma Process 5:211–237. https://doi.org/10.1007/BF00615122

45. Murphy AB (2000) Transport coefficients of hydrogen and argon-hydrogen plasmas. Plasma Chem Plasma Process 20:279–297. https://doi.org/10.1023/A:1007099926249

46. Baeva M, Zhu T, Kewitz T, Testrich H, Foest R (2021) Self-consistent cathode-plasma coupling and role of the fluid flow approach in torch modeling. J Therm Spray Technol 30:1737–1750. https://doi.org/10.1007/s11666-021-01261-4

47. F4MB-XL BRO-0006.6 Atmospheric Plasma Spray Solutions (2016) Oerlikon Metco, Switzerland. https://www.oerlikon.com/metco/de/medien/downloadcenter/?type=brochures. Accessed 22 May 2022

48. Talbot L, Cheng RK, Schefer RW, Willis DR (1980) Thermophoresis of particles in a heated boundary layer. J Fluid Mech 101:737–758. https://doi.org/10.1017/S0022112080001905

49. Ranz WE, Marshall WR (1952) Evaporation from Drops. Chem Eng Prog 48:141–146

50. Huang PC, Heberlein JVR, Pfender E (1995) Particle behavior in a two-fluid turbulent plasma jet. Surf Coat Technol 73:142–151. https://doi.org/10.1016/0257-8972(94)02382-4
51. Escure C, Vardelle M, Fauchais P (2003) Experimental and theoretical study of the impact of alumina droplets on cold and hot substrates. Plasma Chem Plasma Process 23:185–221. https://doi.org/10.1023/A:1022976914185
52. Langstaff D, Gunn M, Greaves GN, Marsing A, Kargl F (2013) Aerodynamic levitator furnace for measuring thermophysical properties of refractory liquids. Rev Sci Instrum 84:124901. https://doi.org/10.1063/1.4832115
53. Ohishi Y, Kargl F, Nakamori F, Muta H, Kurosaki K, Yamanaka S (2017) Physical properties of core-concrete systems: Al$_2$O$_3$-ZrO$_2$ molten materials measured by aerodynamic levitation. J Nucl Mater 487:121–127. https://doi.org/10.1016/j.jnucmat.2017.02.002
54. Wilcox DC (1998) Turbulence modeling for CFD. La Canada
55. Bobzin K, Öte M, Schein J, Zimmermann S, Möhwald K, Lummer C (2016) Modelling the plasma jet in multi-arc plasma spraying. J Therm Spray Technol 25:1111–1126. https://doi.org/10.1007/s11666-016-0438-0
56. Shigeta M (2019) Modeling and simulation of a turbulent-like thermal plasma jet for nanopowder production. IEEJ Trans Electr Electron Eng 14:16–28. https://doi.org/10.1002/tee.22761
57. Comsol documentation: theory for the particle tracing for fluid flow interface (2020) Stockholm, Sweden. https://doc.comsol.com/5.6/docserver/#!/com.comsol.help.particle/particle_ug_fluid_flow.08.36.html. Accessed 22 May 2022
58. Flórez-Orrego D, Arias W, López D, Velásquez H (2012) Experimental and CFD study of a single phase cone-shaped helical coiled heat exchanger: an empirical correlation. In: Proceedings of the 25th international conference on efficiency, cost, optimization, simulation and environmental impact of energy systems
59. Vardelle M, Fauchais P, Vardelle A, Li KI, Dussoubs B, Themelis NJ (2001) Controlling particle injection in plasma spraying. J Therm Spray Technol 10:267–284. https://doi.org/10.1361/105996301770349367
60. Njah Z, Mostaghimi J, Faghri M, Boulos M (1993) Study of 3-D mixing of a cold jet with a transverse plasma stream. Int J Heat Mass Transf 36:3897–3907. https://doi.org/10.1016/0017-9310(93)90140-2
61. Thermal spray monitoring solution (2022) Montreal, Canada. https://tecnar.com/wp-content/themes/tecnar-oz/. Accessed 22 May 2022
62. Zhu T, Baeva M, Testrich H, Kewitz K, Foest R (2022) Effect of a spatially fluctuating heating of particles in a plasma spray process. Dataset, INPTDAT. https://doi.org/10.34711/INPTDAT.571
63. Static light scattering (2022) Malvern, UK. https://www.malvernpanalytical.com/. Accessed 22 May 2022
64. Huang PC, Heberlein JVR, Pfender E (1995) A two-fluid model of turbulence for a thermal plasma jet. Plasma Chem Plasma Process 15:25–46. https://doi.org/10.1007/BF01596680
65. Zhang H, Hu S, Wang G (2006) Simulation of powder transport in plasma jet via hybrid Lattice Boltzmann method and probabilistic algorithm. Surf Coat Technol 201:886–894. https://doi.org/10.1016/j.surfcoat.2006.01.006
66. Djebali R, El Ganaoui M, Pateyron B (2012) A lattice Boltzmann-based investigation of powder in-flight characteristics during APS process, part I: modelling and validation. Prog Comput Fluid Dyn 12:270–278. https://doi.org/10.1504/PCFD.2012.048250
67. Software assistant for thermal spray coating (2009) University of Limoges, Limoges. Jets&Poudres (free.fr). Accessed 22 May 2022
68. Pfender E, Chang CH (1998) Plasma spray jets and plasma-particulate interaction: modeling and experiments. In: International thermal spray conference proceedings, pp 315–327. https://doi.org/10.31399/asm.cp.itsc1998p0315
69. Sun YZ, Dang YB (2011) Numerical simulation of atmospheric pressure plasma jet using Lattice Boltzmann method. Appl Mech Mater 44:1838–1842. https://doi.org/10.4028/www.scientific.net/AMM.44-47.1838
70. Menart J, Malik S (2002) Net emission coefficients for argon-iron thermal plasmas. J Phys D: Appl Physic 35:867–874. https://doi.org/10.1088/0022-3727/35/9/306
71. Cressault Y, Rouffet ME, Gleizes A, Meillot E (2010) Net emission of Ar-H$_2$-He thermal plasmas at atmospheric pressure. J Phys D: Appl Phys 43:335204. https://doi.org/10.1088/0022-3727/43/33/335204